Predicting Antenna Noise Temperature Due to Rain Clouds at Microwave and Millimeter-Wave Frequencies

Frank S. Marzano, *Senior Member, IEEE*

***Abstract*—Model-oriented methods to predict antenna noise temperature due to rainfall along slant paths are developed and illustrated for communication systems at Ka-band and above. The adopted Sky Noise Eddington Model (SNEM) relies on an accurate analytical solution of the radiative transfer equation and on stratiform and convective rainfall stratified structures, synthetically generated from cloud-resolving model statistics. The approach to predict antenna noise temperature is based on the multiple regression analysis, trained by SNEM-derived cloud radiative data sets, and can handle either slant-path attenuation or columnar liquid water or rain rate as input predictors. Statistical scaling with respect to frequency and zenith angle is also analyzed and modeled in the microwave and millimeter-wave range. In order to test the proposed prediction technique, measurements of the ITALSAT satellite ground-station at Pomezia (Rome, Italy) are taken into consideration for two case studies. Combined data from the ITALSAT three-beacon receiver at 18.7, 39.6, and 49.5 GHz and from a three-channel microwave radiometer at 13.0, 23.8, and 31.6 GHz are processed. Results are shown and discussed in terms of antenna noise temperature estimation by using the satellite-beacon path attenuation as predicting variable.**

***Index Terms*—Antenna noise temperature, prediction methods, radio propagation, rainfall, sky-noise models.**

I. Introduction

FREQUENCIES at Ka-band and above, with a special attention to millimeter-wave carriers, are becoming increasingly investigated in communication link designs due to their appealing features in terms of fractional bandwidth and still open availability [1]–[3]. The optimal allocation of channel resources above Ku-band is limited by the significant impact of radio-meteorological factors which can irremediably degrade the quality of service for fairly high percentage of time [4], [5]. The major cause of outages at Ka-band and above is not only convective rainfall, as for lower frequencies, but even nonprecipitating clouds and moderate precipitation produced by stratiform clouds [6]–[8]. This scenario prompts for devising adequate fade mitigation techniques and for evaluating and predicting the atmospheric effects in a more and more accurate way (e.g., [9] and [10]).

Manuscript received August 14, 2006; revised December 27, 2006. This work was supported in part by the Italian Department of Civil Protection, Rome, Italy, Region Abruzzo, Italy, and the Italian Space Agency, Rome.

The author is with the Department of Electronic Engineering, University of Rome La Sapienza, Rome, Italy, and the Center of Excellence CETEMPS, University of L'Aquila, Italy (e-mail: marzano@die.uniroma1.it).

Color versions of one or more of the figures in this paper are available online at http://ieeexplore.ieee.org.

Digital Object Identifier 10.1109/TAP.2007.900252

Channel characterization and modeling above Ku-band may be extremely important for very small aperture terminals (VSATs), for point-to-multipoint networks, and, in general, for low-fade margin systems [3], [11]. In this respect, antenna noise temperature can play a significant role in the link budget design, especially when low margins and optimal channel capacity are foreseen as coupled constraints [9], [12]. Nowadays technology permits the design of very low-noise receivers, which allow relatively high bit rates for VSATs [11]. For marginal carrier-to-noise (C/N) ratio, the system equivalent noise temperature decreases and the impact of atmospheric noise temperature can become nonnegligible [13]. An appealing goal for design purposes could be to predict antenna noise temperature due to rain clouds in an adaptive mode, and possibly on short to medium time scales, from measurements of path attenuation or from available meteorological data [14], [15].

Simplified empirical-statistical prediction models of radio-meteorological effects are not always suitable when extrapolated to short-term time scales and to millimeter-wave frequencies [16]. Experimental characterization of atmospheric radio-propagation effects along satellite links is of major importance for model testing but is very often unfeasible and costly (e.g., [17] and [18]). The alternative choice is to adopt a physical approach to the modeling of atmospheric fade, noise, and dynamics [19] even though, subject to the validity domain of the model itself, the physical approach can offer a thorough insight into radiowave propagation trough atmosphere (e.g., [20]). A physically based method can also give a better understanding and evaluation of propagation phenomena due to clouds and rainfall. Hydrometeor multiple scattering should be taken into account when incoherent effects due to rain and ice multiple scattering are involved, especially at frequencies at Ka-band and above [13], [21].

The increasing use of colocated microwave radiometers in synergy with satellite beacon receivers has renewed the interest in measuring and modeling the sky-noise antenna temperature [12]. A previous work was devoted to set up a rigorous simplified theoretical framework for describing antenna noise temperature and to propose radiative models of clouds and rainfall [22]. The antenna noise temperature was analytically expressed by resorting to the sky-noise Eddington model solution of the radiative transfer equation for plane-parallel atmosphere geometry. Physical-statistical stratified models of clouds and rainfall were also described in terms of antenna noise temperature signatures.

This paper is aimed at exploiting these physically oriented rain-cloud radiative models to:

i) show the limitation of assuming a constant value for the mean radiative (or effective) temperature T_m and analyze the sensitivity of T_m to rainfall model parameters;
ii) predict T_m due to convective and stratiform rainfall from either path attenuation or columnar liquid water content or rain-rate measurements in order to parameterize the antenna noise expression within the link budget design;
iii) characterize the frequency and angle scaling properties of T_m due to rain clouds;
iv) test the physically oriented prediction methods with available satellite-link data at Ka-band and above.

This paper is organized as follows. In Section II, the analytical modeling of the antenna noise temperature is summarized and a sensitivity study carried out. Section III is devoted to the design of statistical prediction techniques of sky noise temperature with applications to frequency and angle scaling. In Section IV, two case studies are analyzed by using the proposed physically oriented estimation method.

II. Modeling Rainfall Antenna Noise Temperature

In the following sections we will introduce general expressions of the effective temperature due to a scattering atmosphere for ground-based antenna observations. We will also verify whether some theoretical simplifications can still yield accurate results and show numerical results.

A. Analytical Model of Effective Mean Temperature

For ground-based measurements of sky noise antenna temperature within a vertically stratified atmosphere, it is convenient to express the received brightness temperature T_B through the *effective mean (radiative) temperature* T_m [19]

$$\begin{aligned} T_B(z=0,\theta) &= T_m(z=0,\theta)\left(1-e^{-\tau/\mu_0}\right)+T_c e^{-\tau/\mu_0} \\ &= T_m(z=0,\theta)(1-10^{-A})+T_c 10^{-A} \\ &\cong T_A(z=0,\theta) \end{aligned} \tag{1}$$

where $z=0$ stands for surface height, τ is the vertical optical thickness (due to both absorption and scattering), $\mu_{\rm O}=cos\theta$ with θ the observation zenith angle, A is the slant-path attenuation (with $A=4.343\tau/\mu_o$ in decibels), and T_c is the microwave cosmic T_B (with $T_c \cong 2.73$ K). Note that both T_m and τ by definition depend on frequency and hydrometeor content on their turn. The impact of the antenna radiation pattern is generally less than 0.5% in rainy conditions so that we can substitute the antenna noise temperature T_A with the brightness temperature T_B, as in the last term of (1) [22]. By inverting (1), we can derive the following definition for T_m:

$$T_m(z=0,\theta) \equiv \frac{T_B(z=0,\theta)-T_c e^{-\tau/\mu_0}}{1-e^{-\tau/\mu_0}}. \tag{2}$$

It is apparent from (2) that T_m does not necessarily coincide with the thermodynamic temperature of the atmosphere but takes into account, in a frequency-dependent way, both radiative and observation parameters. From (2), the atmospheric slant-path attenuation A can be also derived from T_m and radiometric measurements of T_B

$$\begin{aligned} A(z=0,\theta) &= \frac{4.343}{\mu_0}\tau \\ &= \ln\left(\frac{T_m(z=0,\theta)-T_c}{T_m(z=0,\theta)-T_B(z=0,\theta)}\right). \end{aligned} \tag{3}$$

In order to handle (1) and (3) using only either A or T_B measurements, respectively, a simple way is to resort to the ITU-R approximate model [16], [11]. The latter is such that T_m is supposed to be constant

$$T_m(z=0,\theta,\nu)=T_0 \tag{4}$$

where the value $T_0 \cong 275$ K is suggested [16].

Indeed, (4) is a very crude approximation for T_m. To realize it, we can consider the general theoretical framework of the sky noise Eddington model (SNEM), extensively described in [22]. The basic assumption of SNEM is to expand $T_B(z,\theta)$ in terms of Legendre polynomials with respect to $\mu=\cos\theta$ up to the first order, deriving the expansion coefficients from the solution of the radiative transfer integro-differential equation [22]. In case of a homogeneous atmospheric slab with $\tau=\tau_s$ its total optical thickness and a temperature linear decrement, it is quite straightforward to derive the following closed-form expression for the ground-based effective mean temperature:

$$\begin{aligned} &T_m(z=0,\theta) \\ &\quad=\left[t_0-t_1\mu_0-\frac{wg\mu_0}{(1-wg)}t_1\right] \\ &\qquad+\frac{1}{1-e^{-\tau_s/\mu}}\left[t_1\tau_s-wC_1\frac{1+c\mu_0 g}{1-\lambda\mu_0}(e^{-}\tau_s/\mu_0-e^{-}\lambda\tau_s)\right. \\ &\qquad\qquad\left.+-wC_2\frac{1-c\mu_0 g}{1+\lambda\mu_0}(e^{-\tau_s/\mu_0}-e^{\lambda\tau_s})\right] \end{aligned} \tag{5}$$

where C_1 and C_2 are the integration constants, derived from the imposition of the boundary conditions, and t_0 and t_1 are the temperature decrease intercept and slope (with respect to the optical thickness τ), respectively. The quantity λ is a known eigenvalue, expressed in terms of volumetric albedo w (i.e., scattering over extinction coefficient) and the scattering asymmetry factor g [22]. Overall errors of (5) have been found to be less than 1% when compared to fully numerical solutions of the radiative transfer equation. Previous results in (5) can be generalized to an inhomogeneous planar atmosphere by adopting a recursive approach [22].

If the albedo w is zero in (5) (i.e., the atmosphere is not scattering), then T_m can be expressed as

$$T_m(z=0,\theta)=[t_0-t_1\mu_0]+\left[\frac{t_1\tau_s}{1-e^{-\tau_s/\mu_0}}\right]. \tag{6}$$

Finally, in case of thermally uniform nonscattering slab at temperature T_0, then it results $t_0=T_0, t_1=0$, $w=0$ and $g=0$. Then, from (6), we can derive the approximate formula (4), i.e., $T_m(z=0,\theta)=T_0$. Previous considerations may give a hint on the theoretical validity of the ITU-R atmospheric sky-noise model, given in (4).

B. Numerical Sensitivity Analysis

Equation (5) of T_m indicates that the effective mean temperature is a complicate function of optical parameters that, in turn, depend on hydrometeor distribution. We can exploit (5) to analyze its sensitivity to these parameters.

In order to compute the rainfall optical parameters, i.e., τ, w, and g, we need to specify the particle size distribution (PSD) of sphere-equivalent hydrometeors. Their experimental PSDs can be parameterized with respect to the liquid and ice hydrometeor contents L of a vertical rain cloud structure [21], [22]. The latter may be obtained from a synthetic rain-cloud generator, whose statistics in terms of hydrometeor content mean profile and correlation matrix is derived from numerical cloud-resolving model outputs and classified with respect to clear air (Ca), nonprecipitating cloud (Cl), stratiform rain (Ns, nimbostratus), and convective rain (Cb, cumulonimbus) [22]. The vertical structure may be parameterized to the surface temperature, humidity, and pressure values and their vertical gradients whose values are assumed randomly determined within a prescribed uniform distribution.

Within the context of SNEM model applications, only an example of a spring rain-cloud data set is here taken into consideration. Mean surface data were set to 22 °C for temperature, 1010 mbar for pressure, and 90% for relative humidity, while vertical gradients were set to 6.5 K/km for a linear temperature decrease, to 1.3 km for inverse-exponential humidity decrease, and to 7 km for inverse-exponential pressure decrease. The input data set consists of 5000 simulations of columnar (vertically integrated) nonprecipitating liquid (i.e., cloud droplets), precipitating liquid (i.e., rain), nonprecipitating ice (i.e., crystals), and precipitating ice (i.e., graupel) associated to antenna noise temperatures T_A for ground-based antennas, related effective mean temperatures T_m and slant-path attenuations A at a given elevation and for several microwave radio propagation and radiometric frequencies between 10 and 90 GHz. The channel set, used here, lists the following central frequencies: 13.00, 18.60, 20.60, 23.80, 31.65, 36.50, 50.20, 53.80, and 85.0 GHz for sky-noise simulations and 12.50, 18.68, 29.65, 39.59, 49.49, and 90.0 GHz for communication purposes. Elevation angles between 10° and 90° have been also considered.

It is worth mentioning that the same SNEM-based synthetic radiative data set can be generated for surface and meteorological conditions typical of different seasons and climates. The generalization to various climatic conditions could be accomplished by first adapting the meteorological and environmental conditions that influence the vertical composition of rain clouds. The impact of climatic conditions on the rain-cloud structure could be then modified by assuming an a priori hydrometeor average vertical profile and, possibly, a related correlation matrix. To a first approximation, the latter could be let unchanged with respect to the climatic variation by assuming an "intrinsic" rain-cloud vertical correlation matrix, distinguished only by rain-cloud class membership.

As an example of SNEM-derived data set, Fig. 1 shows the sky-noise effective temperature T_m at 45° zenith angle and at 18.7 and 39.6 GHz for ground-based antennas over a land surface for Ns and Cb genera as function of the slant path attenuation A, columnar liquid water content L, and surface rain rate R. The stronger the rain regime is, the quicker the saturation of effective temperature is. For Ns, the relation between A and T_m denotes an initial saturation effect only beyond 10 dB of attenuation. For Cb convective rain, the frequency dependence is almost lost for attenuations larger than 15 dB or columnar water larger than 2 kg/m ^{2} when rainfall becomes a sort of black body observed from ground. The dynamic range of A is, of course, strongly frequency-dependent with values of A not larger than 4 dB and at 18.7 GHz and 45 dB at 39.6 GHz. The correlation between T_m and R is relatively low for Ns, whereas for Cb a saturation of T_m is noted for $R > 40$ mm/h.

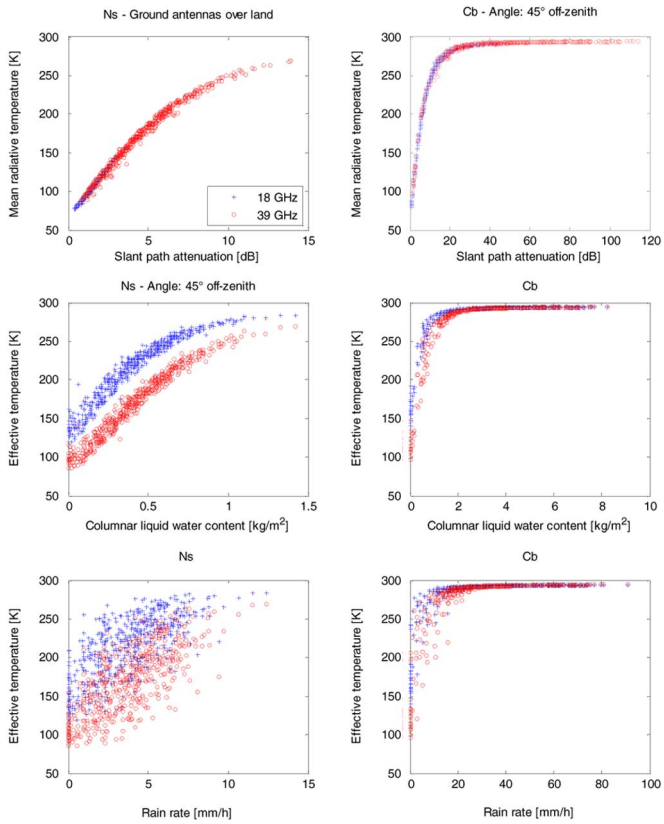

Fig. 1. Sky-noise effective mean temperature T_m at 45° zenith angle and at 18.7 and 39.6 GHz for ground-based antennas over a land surface, simulated for Ns (left panels) and Cb genera (right panels) as a function of path attenuation A, columnar liquid water L content, and rain-rate R.

The effects of precipitating ice on sky-noise temperature may be noticeable, even though thermal emission is basically driven by liquid water hydrometeors. This is due to the significant scattering effect of ice particles, weighted by their albedo [13], [22]. In order to quantify these considerations, we can define the percentage errors shown in (7) and (8) at the bottom of the following page, where we have explicated the dependence of T_m on w, g, τ, and L and the "tilde" stands for the modified variable. The error ε_w evaluates the effect of $w = 0$, whereas ε_L is the effect of considering only liquid hydrometeors (i.e., $L = L_{\text{liq}}$).

Fig. 2 shows the percentage errors (8) at 45° zenith angle and at 18.7 and 39.6 GHz for ground-based antennas over a land surface, as a function of slant path attenuation. For Ns rain

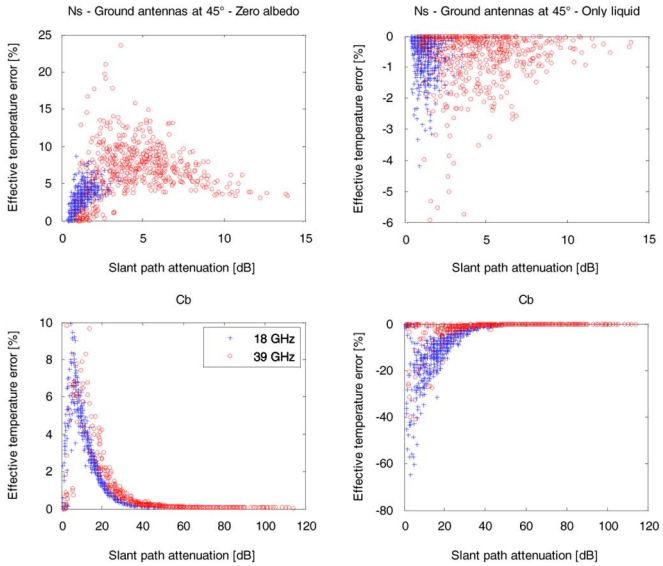

Fig. 2. Percentage errors of sky-noise effective temperature at 45° zenith angle and at 18.7 and 39.6 GHz for ground-based antennas over a Lambertian land surface for Ns and Cb as a function of the slant path attenuation. Left panels refer to the assumption of zero volumetric albedo for all hydrometeors, whereas right panels refer to zero ice hydrometeor content.

clouds, which are mostly made by raindrops, the effect of neglecting the ice can give small errors up to 5–10%, whereas a more significant impact is due to setting the albedo to zero. For Cb rain clouds, the ice hydrometeor effects are relevant with errors up to 50%, especially for medium-to-high path attenuation and higher frequencies. A zero-error limit is clear at 39.6 GHz for $A > 30$ dB due to saturation effects. An analogous sensitivity analysis with respect to the asymmetry factor g shows that the overall errors are always less than 5% percent for Ns and Cb at 18.7 and 39.6 GHz. For nonprecipitating clouds, the errors may become nonnegligible only at W-band, as expected from frequency-scaling properties of the atmospheric opacity.

For ground-based observations, the use of ITU-R formula with $T_m = 275$ K, as in (4) would give errors much larger at 18.7 GHz than at 39.7 GHz, as noted in Fig. 3 due to less pronounced saturation effects in the $T_m - A$ relation at lower frequencies. The underestimation errors at 18.7 GHz can be as low as -70% for low path attenuation, whereas at 39.7 GHz errors may reach -40% for Cb and $A < 20$ dB.

III. Predicting Antenna Noise Temperature

In this section, we will design and optimize the statistical prediction algorithms. The focus will be also placed on the scaling properties of the sky-noise effective temperature.

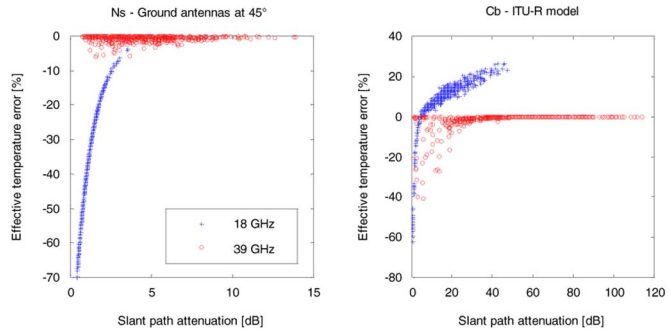

Fig. 3. Same as in Fig. 2 but assuming a constant $T_m = 275$ K as suggested by ITU-R.

A. Statistical Prediction of Rainfall Effective Temperature

Synthetic cloud radiative data sets, generated by SNEM, can be used for developing physically oriented statistical prediction techniques. Within this simulation environment, we can perform such analysis by assuming that the random variability of the radio-propagation process through a rain cloud is well (and realistically) represented by the synthetic radio-propagation data set [22]. As already mentioned, these results would be generally valid only for environmental conditions and antenna configurations assumed within the model itself, but this would be similarly true for a specific experimental analysis as well. More importantly, the synthetic data set offers several parameters to be tuned to a given measuring station.

In order to set up a model-based statistical predictor, we may assume to have, as inputs, different sets of parameters:

1) path attenuation $A(\nu, \theta)$ at given frequency ν and angle θ, available from ground-based receiver measurements;
2) measured surface rain rate R, available from rain-gauge or disdrometer measurements;
3) columnar liquid water content L, available either from meteorological forecast numerical model outputs or from ground-based radiometer measurements.

A combination of the previous parameters can be also taken into consideration within a measured predictor vector **x**. The statistical predictor can be designed as an algorithm with two successive stages. First of all, we can identify the observed meteorological situation, e.g., in terms of clear, cloudy, or rainy conditions. Then, we can estimate the radio-propagation parameter of interest, such as T_m.

A way to approach the problem of rain class recognition is to resort to the maximum likelihood (ML) technique by assuming a multidimensional Gaussian metrics for the difference between the measured quantities, expressed by a vector **x,** and their known mean value or centroids $< \mathbf{x}_c >$ [23]. Thus, the

$$\varepsilon_w = 100 \frac{\tilde{T}_m(z=0,\theta; w=0, g, \tau, L) - T_m(z=0,\theta; w, g, \tau, L)}{T_m(z=0,\theta; w, g, \tau, L)} \tag{7}$$

$$\varepsilon_L = 100 \frac{\tilde{T}_m(z=0,\theta; w, g, \tau, L=L_{\text{liq}}) - T_m(z=0,\theta; w, g, \tau, L)}{T_m(z=0,\theta; w, g, \tau, L)} \tag{8}$$

TABLE I
CLASS CENTROIDS IN TERMS OF SLANT-PATH ATTENUATION AT 45° ELEVATION FOR CA, CL, NS, AND CB IN A MIDSEASON CLIMATE

A [dB]: centroids	18.7 GHz	39.6 GHz	49.5 GHz
Clear air	0.278	0.585	1.969
Cloud	0.345	0.911	2.162
Nimbostratus	1.038	4.211	7.051
Cumulonimbus	8.532	29.030	38.116

first ML stage consists of maximizing a proper norm or distance function $d(c)$ with respect to the class c

$$\hat{c} = \mathrm{ML}_c[d(c)] = \mathrm{ML}_c\left[-\sqrt{(\mathbf{x}- < \mathbf{x}_c >)^T[\mathbf{C}_{\mathrm{xc}}]^{-1}(\mathbf{x}- < \mathbf{x}_c >)}\right] \quad (9)$$

where c may be equal to Ca (clear air), Cl (nonprecipitating clouds), Ns (nimbostratus), or Cb (cumulonimbus). The matrices $\mathbf{C}_{\mathrm{xc}}$ are the class autocovariance matrices of each class c. The superscripts "T" and "-1" indicate matrix transpose and inversion, respectively, whereas ML_c is a functional that returns the value of c corresponding to the maximum of $d(c)$.

Examples of class centroids are given in Table I in terms of slant path attenuation at 45° elevation for Ca, Cl, Ns, and Cb, using the SNEM midseason data set previously described. The autocovariance matrices $\mathbf{C}_{\mathrm{xc}}$ of each class can be computed from the same data set as well.

Once rain conditions have been identified, we can proceed to predict the sky-noise effective mean temperature. A nonlinear regression approach has been chosen here by adopting a polynomial model. Regression techniques are fairly well suited to this aim, as they are both simple to handle and can be generalized in order to perform a robust estimation in presence of unexpected noise and errors [24]. For ground-based antennas, the prediction models of T_m can be stated in different manners, e.g., with respect to predictors A, L, or R belonging to an estimated class c as shown in (10) at the bottom of the page, where ν_k is the kth frequency and J, L, and N are the polynomial maximum orders. The following units hold for (10): T_m[K], A [dB], L [kg ·m^{-2}] and R [mm·h $^{-1}$]. The previous formulas can be easily extended to a combination of the available predictors. If $K = 1$, (10) reduces to an estimate of T_m using the cofrequency path attenuation.

The coefficients are dependent on the observation angle and frequency. They can be estimated by employing again the SNEM-derived cloud radiative data set, previously described. To this aim, we have divided the midseason data set into a train and test set, adding to simulated T_As a Gaussian noise with a zero mean and a standard deviation equal to 1 K. For $K = 1$ and $\nu = \nu_1$, polynomial regression models with various J, L, and N have been compared to power-law relations in terms of root mean square errors (RMSEs). The output of this optimization procedure has suggested the choice of a cubic function (i.e., $J = 3, L = 3$ and $N = 3$) for all three models in (10).

TABLE II
CUBIC REGRESSION COEFFICIENTS OF (10) FOR NS AND CB AT 18.7 AND 39.6 GHZ AT 45° FOR A MIDSEASON DATA SET TOGETHER WITH RMSES, GIVEN IN K. RESULTS FOR CB ARE VALID FOR $R > 10$ mm/h

T_m [K]	Ns		Cb	
	18.7 GHz	39.6 GHz	18.7 GHz	39.6 GHz
a_0	72.9647	64.6964	106.7186	225.4640
a_1	14.6261	28.9851	19.1822	3.4444
a_2	5.7085	-1.0800	-0.6556	-0.0542
a_3	-0.9146	0.0031	0.0072	0.0003
RMSE	2.7	4.7	6.0	11.8
b_0	75.6557	74.4539	29.8581	205.2246
b_1	22.3167	127.2115	124.8401	51.4969
b_2	0.4230	-23.1472	-19.7491	-9.4235
b_3	0.4132	0.7121	1.0211	0.5415
RMSE	6.2	17.7	11.6	11.5
d_0	82.2646	110.5684	106.2583	237.9072
d_1	4.7295	22.0927	9.5560	3.5984
d_2	-0.3004	-1.6542	-0.1647	-0.0726
d_3	0.0328	0.0728	0.0009	0.0005
RMSE	8.7	28.5	18.4	13.5

The obtained coefficients in (10) are reported in Table II for Ns and Cb clouds and at 18.7 and 39.6 GHz and for 45° elevation angle, as an example. The analysis of the table RMSEs confirms what was already noted in Fig. 1.

i) The effective mean temperature is highly correlated with path attenuation, and this provides a fairly accurate prediction.
ii) Saturation effects for $A - T_m$ are responsible for larger errors at 39.7 GHz in case of high rain rates.
iii) Estimates of T_m are less accurate when using R as a predictor since R is poorly correlated with T_m.

The last comment can be further deepened by noting that R is a near-surface parameter, whereas both A and L are vertically integrated parameters highly correlated to T_A, and then T_m, measurements.

B. Scaling Properties of Rainfall Effective Temperature

A major issue of the link budget design for innovative satellite applications is the ability to scale, in both frequency and angle, the propagation characteristics known at other frequencies and/or pointing angles [12], [19]. Even if the analytical solution of (5) suggests a complicate dependence of T_m on θ and ν (through μ, w, g, and τ), the analysis of Fig. 1 reveals that statistical laws can be extracted from the SNEM simulation ensemble. This is, in a way, similar to the experimental approach where the procedure is to acquire radio-propagation measurements at several frequencies and angles and then to look for a best fitting curve (e.g., [18]).

$$\begin{cases} \hat{T}_m(z=0,\theta,\nu;\hat{c}) = a_0 + \sum_{j=1}^{J}\left\{\sum_{k=1}^{K} a_{\mathrm{jk}}[A(\theta,\nu_k;\hat{c})]^j\right\} \\ \hat{T}_m(z=0,\theta,\nu;\hat{c}) = b_0 + \sum_{l=1}^{L} b_l[L(\hat{c})]^l \\ \hat{T}_m(z=0,\theta,\nu;\hat{c}) = d_0 + \sum_{n=1}^{N} d_n[R(\hat{c})]^n \end{cases} \quad (10)$$

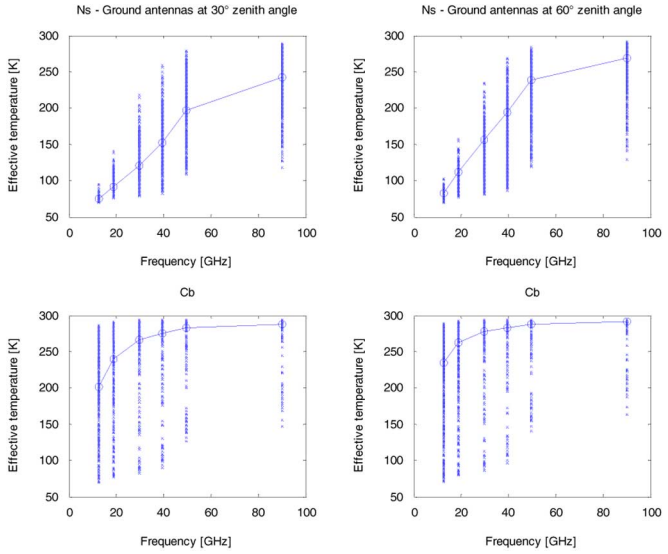

Fig. 4. Effective temperature variability at 30° (left panels) and 60° (right panels) elevation angle for Ns (top panels) and Cb genera (bottom panels) as a function of microwave frequency between 10 and 90 GHz. The solid lines connect the mean values at each discrete frequency.

TABLE III
POWER-LAW REGRESSION COEFFICIENTS OF (11) FOR NS AND CB AT 30°, 45°, AND 60° ZENITH ANGLE FOR A MIDSEASON DATA SET. RMSES, GIVEN IN K, ARE ALSO REPORTED

Average T_m *[K]*	Ns			Cb		
	θ=30°	θ=45°	θ=60°	θ=30°	θ=45°	θ=60°
a_v	15.04	15.43	17.55	139.95	159.31	189.12
b_v	0.6289	0.6411	0.6366	0.1745	0.1444	0.1044
RMSE	12.8	16.0	21.8	13.6	11.7	8.6

Fig. 4 shows the effective mean temperature T_m at 30° and 60° elevation angle for Ns and Cb genera as a function of microwave frequency between 10 and 90 GHz. The solid lines connect the mean values at each discrete frequency in order to appreciate the average frequency scaling. As expected, there is an increase of T_m with frequency, due to the increase of atmospheric path attenuation and multiple scattering. This behavior is also dependent on the zenith angle, the dynamic range of T_m being larger for higher zenith angles. The fact that the interpolation line of the frequency scaling does not pass through the center of each frequency-dependent data set is explained by noting that the density distribution of T_m is not uniform within its range limits at a given frequency.

The results of Fig. 4 suggest modeling the frequency scaling of the average behavior (indicated by an "overbar") of T_m by means of a power-law relation

$$\bar{T}_m(z=0,\theta,\upsilon) = a_\nu \nu^{b_\nu} \tag{11}$$

where a_ν and b_ν are the frequency scaling coefficients which are meteorologically and angularly dependent. Table III provides the regression coefficients of (11) with relative RMSE at 30°, 45°, and 60° zenith-angle observation between 10–90 GHz, derived from the SNEM midseason data set.

TABLE IV
POWER-LAW REGRESSION COEFFICIENTS OF (12) FOR NS AND CB AT 18.7, 39.6, AND 49.5 GHZ FOR A MIDSEASON DATA SET. RMSES, GIVEN IN K, ARE ALSO REPORTED

Average T_m *[K]*	Ns			Cb		
	f=18.7	*f*=39.6	*f*=49.5	*f*=18.7	*f*=39.6	*f*=49.5
a_μ	86.44	144.16	188.91	235.49	273.96	281.35
b_μ	-0.3973	-0.3893	-0.2843	-0.1285	-0.0402	-0.0293
RMSE	1.8	1.9	2.6	1.4	0.4	0.3

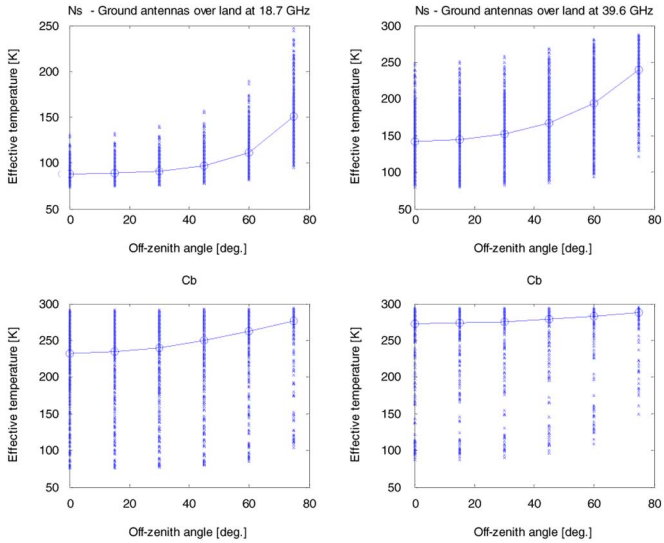

Fig. 5. Effective temperature variability at 18.7 GHz (left panels) and 39.6 GHz (right panels) for Ns (top panels) and Cb genera (bottom panels) as a function of off-zenith angle between 0° and 75°. The solid lines connect the mean values at discrete angles.

The same scaling law of (11) can be exploited for the average angular behavior of T_m at a given frequency ν. In terms of zenith-angle cosine $\mu = \cos\theta$, we may write

$$\bar{T}_m(z=0,\theta,\upsilon) = a_\mu \mu^{b_\mu} \tag{12}$$

where a_μ and b_μ are the angular scaling coefficients, reported in Table IV for the three frequencies at 18.7, 39.7, and 49.5 GHz. Numerical simulations confirm the overall trend assumed in (12). Fig. 5 shows the effective temperature at 18.7 GHz (left panels) and 39.6 GHz (right panels) for Ns (top panels) and Cb genera (bottom panels) as a function of off-zenith angle between 0° and 75°. The solid lines connect the mean values at each discrete angle. As noted for the frequency scaling, the increase of rainfall and frequency band tends to flatten the scaling behavior with respect to the off-zenith angle. The angular dynamic range of T_m is less at 18.7 GHz than at 39.6 GHz, as expected, and, for a given frequency, larger for stratiform than convective rain (e.g., up to 100 K for Ns and up to 30 K for Cb at 39.6 GHz). This average behavior is again explained by considering saturation effects of the receiver response when observing intense rainfall due to larger path attenuation.

IV. Using Experimental Satellite-Link Data

The physically oriented modeling and predictive framework, developed in Section III, can be applied to ground-station measured data. Indeed, the verification of the proposed technique should be carried out by employing a receiver whose antenna noise temperature can be independently evaluated. This kind of measurement is not usually available, unless specifically planned. A way to circumvent this problem is to use measurements derived from colocated radio-link receivers and microwave radiometers, possibly working within frequency bands close to each other and with a similar pointing angle. Again, we could resort to the SNEM synthetic data set to scale in frequency the estimated effective temperature and/or antenna noise temperature. This approach will be the one illustrated in this section to analyze the selected rainfall case studies.

Path-attenuation data acquired at the ITALSAT-satellite ground station located in Pomezia (Rome, Italy) have been used in this paper [12]. From April 1994 to January 2004, measurements of the three ITALSAT-F1 propagation beacons at 18.7, 39.6, and 49.5 GHz have been performed every second at an elevation angle of 41.8° with a receiver antenna of 3.5 m (i.e., beamwidths from 0.2° to 0.5°). The ground station has measured the amplitude and phase of copolar and crosspolar signals at 18.7 and 39.6 GHz and the polarization transfer matrix at 49.5 GHz [25].

Concurrent measurements, performed by two microwave ground-based radiometers (named REC-1 and REC-2) both pointed to the ITALSAT satellite, have been synchronously logged every 4 s by the ITALSAT ground station together with a set of surface meteorological instruments. Radio-sounding meteorological profiles have been also available twice a day with the balloons launched 5 km from the ITALSAT ground station. The radiometer, called REC-2, is a dual-channel system at 23.8 and 31.6 GHz. It consists of a dual-channel offset-fed reflector antenna with a beamwidth of about 1.8° and 1.9° at 23.8 and 31.6 GHz, respectively. Heated air blows across the reflector, preventing the formation of the dew and accumulation of light drizzle, snow, or hail on the reflector surface. The radiometer calibration has been carried out by means of the tipping-curve method, usually once a month. The expected overall radiometric accuracy is about 1 K. The single channel radiometer called REC-1 is an independent system operating at 13.0 GHz. This radiometer has basically the same characteristics of the REC-2 system, but with a larger reflector antenna providing a beamwidth of about 3.5°.

A. ITALSAT Case Studies

In order to show some examples, we have selected two cases of moderate and intense rainfall, observed during April 27 and 29, 1998. A moving average with 1-min window and 1-min sampling period has been applied to analyze raw data of ITALSAT-station instrumentation.

The first case study refers to a moderate rainfall event. Fig. 6 shows the slant path attenuation A at 18.7, 39.6, and 49.5 GHz and antenna noise temperature T_A at 13.0, 23.8, and 31.6 GHz, measured by the beacon receiver and ground-based radiometer at 41.8° elevation angle on April 29, 1998, at 17:00 GMT for about 2 h. The event evolution shows path attenuations and sky-noise temperatures always below 5 dB and 90 K, respectively, except around minute 220, where both A and T_A exhibit a peak at all frequencies. At 18.7 GHz, path attenuation reaches about 5 dB, whereas at 49.5 GHz values, up to 20 dB are measured. Radiometric data range from about 55 K, measured at 13 GHz, to about 200 K at 31.6 GHz. This microwave signature is typical of a cloudy and stratiform rainfall scenario with an embedded more intense episode, probably due to localized convective activity around the minute 220.

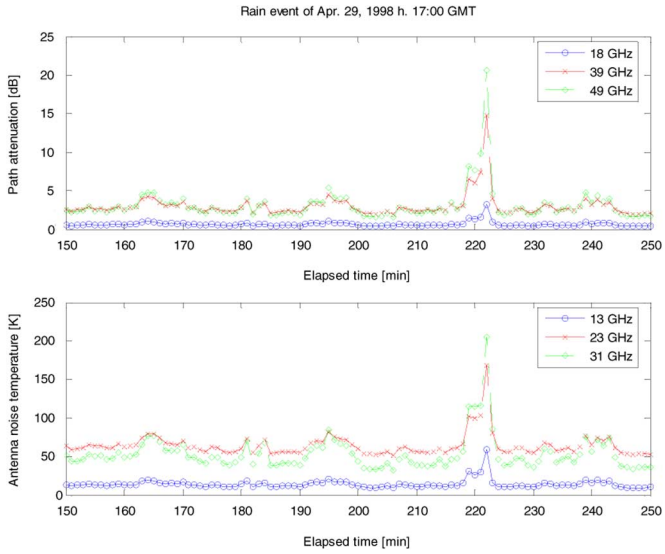

Fig. 6. Slant path attenuation (top panel) at 18.7, 39.6, and 49.5 GHz and brightness temperatures (bottom panel) at 13.0, 23.8, and 31.6 GHz, measured by a beacon receiver and microwave radiometer at 41.8° at the ITALSAT receiving station in Pomezia (Rome, Italy) on April 29, 1998.

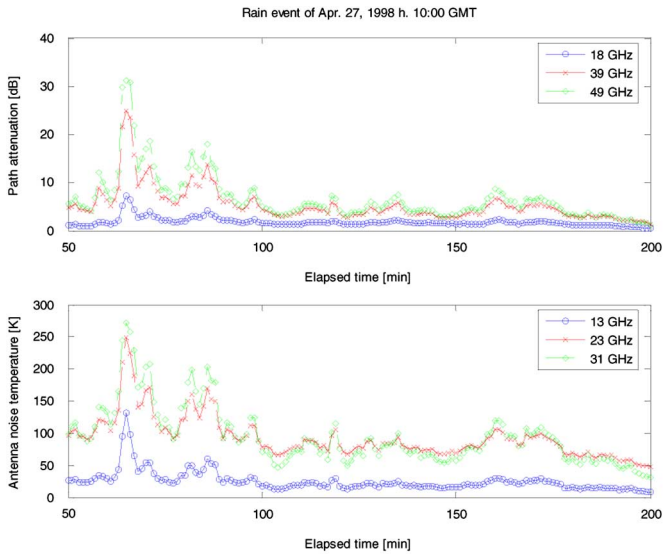

Fig. 7. Same as in Fig. 6 but for the case study on April 27, 1998.

The second case study refers to an intense rainfall occurred on April 27, 1998, at 10:00 GMT for about 2.5 h. Fig. 7 shows the same as in Fig. 6, but for this case study where rainfall occurred between minute 50 and 100 with two distinct episodes of intense rainfall. With respect to Fig. 6, there is a difference in terms of maximum values reached by both path attenuation

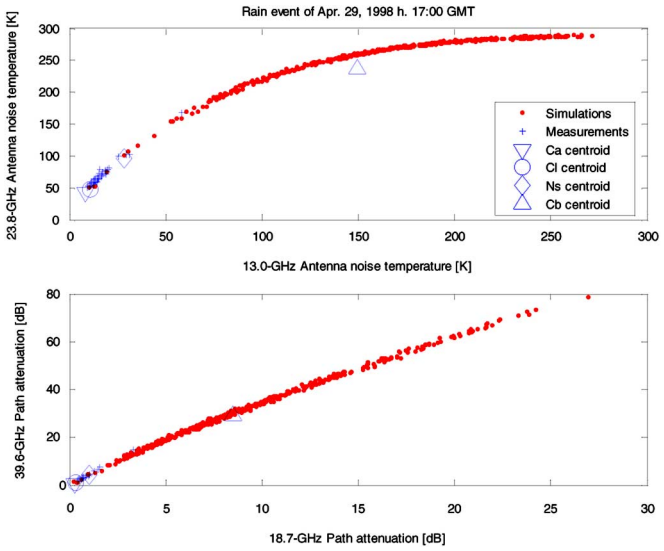

Fig. 8. Comparison between measured and simulated antenna noise temperature (top panels) at 13.0 and 23.8 GHz and path attenuation (bottom panels) at 18.7 and 39.6 GHz for an elevation of 41.8°. Centroids of simulated clear-air (Cl), cloud (Cl), nimbostratus (Ns), and cumulonimbus (Cb) classes are also represented.

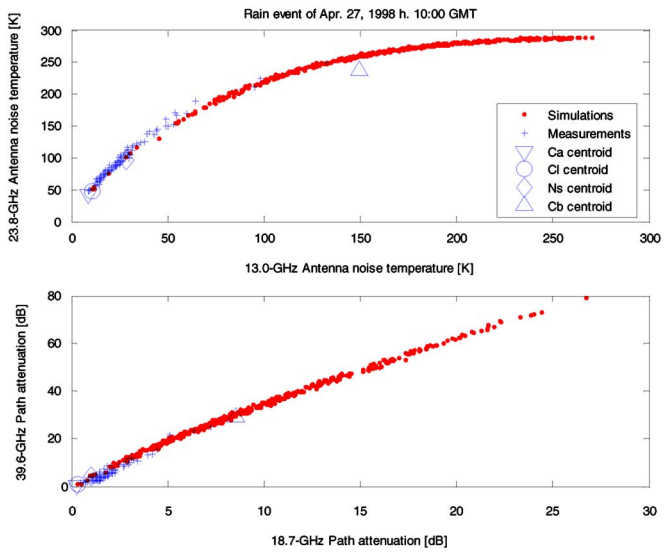

Fig. 9. Same as in Fig. 8 but for the case study on April 27, 1998.

and radiometric measurements during rain. At 18.6 GHz and at 49.5 GHz, path attenuation is as high as 7 and 30 dB, respectively, while radiometric data go from 120 K at 13.0 GHz to 260 K at 31.6 GHz. After minute 100, values of A and T_A are always below 10 dB and 110 K, respectively.

B. Antenna Noise Prediction From Path Attenuation

In order to apply the proposed physically oriented prediction technique, the first step is to classify the rainfall regime of each time step in an automatic way by using (9). In our experimental context, we can set the observation vector $\mathbf{x}$ as the combination of the three ITALSAT measured copolar attenuations, i.e., $\mathbf{x} = [A(\theta, \nu_{18}), A(\theta, \nu_{39}), A(\theta, \nu_{49})]^{\mathrm{T}}$.

To get a qualitative appraisal of the ML classification method, for the case study of April 29, 1998, Fig. 8 shows a comparison between measured and simulated antenna noise temperatures at 13.0 and 23.8 GHz and path attenuations at 18.7 and 39.6 GHz. Centroids of Ca, Cl, Ns, and Cb classes are also superimposed, as derived from Table I but at 41.8° elevation. Even though the classification is carried out in a four-dimensional hyperspace, the figure clearly shows the membership of the rain event, which is basically stratiform. Fig. 9 shows the same as in Fig. 8, but for the case study on April 27, 1998. As expected from the values of the measured A and T_A, this event presents more data classified as convective, embedded in stratiform rain and cloudy conditions.

For both rainfall cases, it is also worth mentioning the fairly good representativeness of SNEM simulations with respect to ITALSAT-station measured data. Indeed, the midseason environmental range assumptions of the synthetic data set have been verified by using available radio-sounding data at 12:00 and 18:00 GMT. By applying (9), we can then convert these qualitative considerations on rainfall type into quantitative classification of each combined measurement time step.

Once each measurement set is classified, the second step is to estimate T_m using (10). Since we have neither measured T_m nor measured T_A of ITALSAT channels, we can retrieve T_A at the available radiometer frequencies for testing purposes. To do this, we can basically use the same polynomial model of (10) adapted to our context, i.e.,

$$\hat{T}_m(z=0,\theta,\nu;\hat{c}) = a_0 + \sum_{j=1}^{3}\left\{\sum_{k=1}^{3} a_{\mathrm{jk}}[A(\theta,\nu_k;\hat{c})]^j\right\} \quad (13)$$

where $\theta = 48.2°$ and v_i is equal to 13.0, 23.8, and 31.6 GHz, and v_k is equal to 18.7, 39.6, and 49.5 GHz. The coefficients a_j have been recomputed, using the same SNEM midseason data set. The obtained RMSE values are lower than those in Table II, as three predictors are used in (13) instead of one.

Fig. 10 illustrates the estimated antenna noise temperature at 13.0, 23.8, and 31.6 GHz, derived from the measured slant-path ITALSAT attenuation by means of (13). Measured antenna noise temperatures are also reported for comparison. Fig. 11 shows the same as in Fig. 10, but for the case study on April 27, 1998.

For the predominantly stratiform event of April 29, the agreement between the estimated and measured antenna noise temperature is fairly good with a trend characterized by an overestimation, especially within the embedded intense portion around minute 220. Overall RMSEs are 2.8, 5.7, and 7.9 K at 13.0, 23.8, and 31.6 GHz, respectively. The more extreme event of April 27 shows higher values of estimated T_A with a good reproduction of the two peaks between minutes 50 and 100. The agreement between the estimated and measured brightness temperature increments is again fairly good with overall RMSE of 7.6, 9.7, and 10.7 K at 13.0, 23.8, and 31.6 GHz, respectively. In both case studies, T_A estimates follow very closely the temporal dynamics of multifrequency antenna noise measurements.

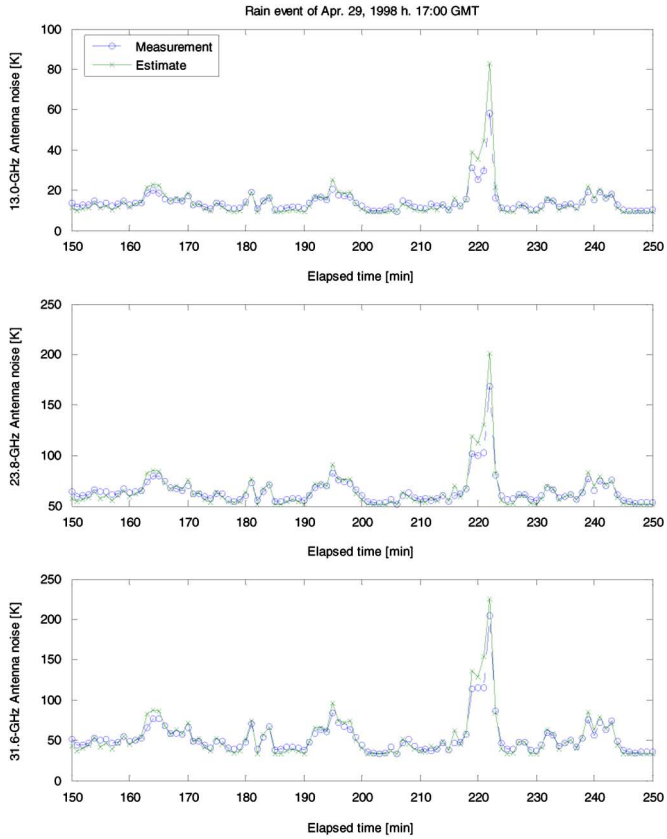

Fig. 10. Estimate of the antenna noise temperature at 13.0, 23.8, and 31.6 GHz from ITALSAT path attenuation measurements on April 29, 1998, at 17:00 GMT. Measurements are also superimposed.

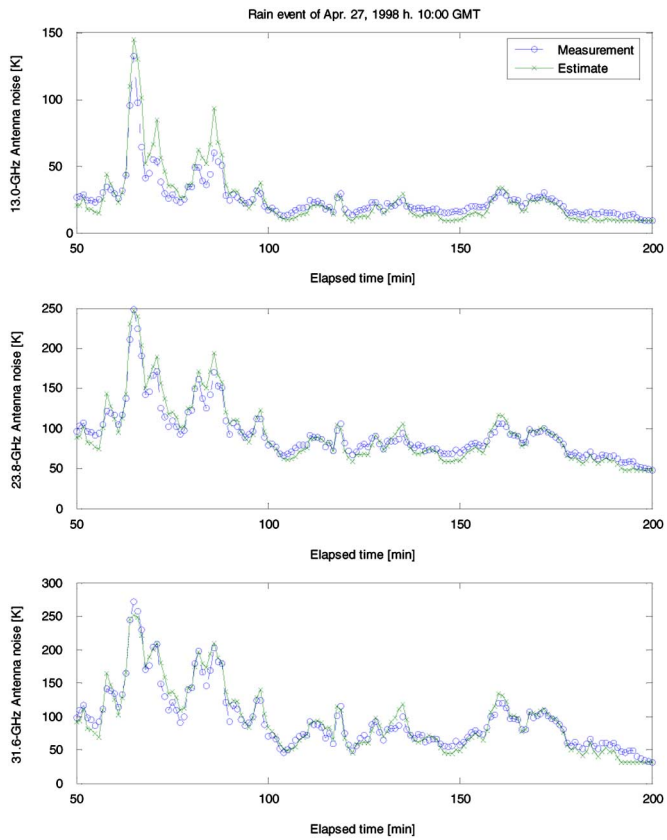

Fig. 11. Same as in Fig. 9 but on April 27, 1998, at 10:00 GMT.

V. Conclusion

Various applications of a physically based antenna noise temperature model, named SNEM and described in a previous paper, to some satellite radio-propagation issues have been illustrated. The effective mean temperature of a rainy atmosphere has been formulated for ground-based antennas and the error budget, due to simplifying assumptions usually applied in practice, has been quantified through a numerical sensitivity analysis. One of the most critical parameterization has been found to be the impact of precipitating ice layers, which cannot be neglected at Ka-band and, in general, for moderate rain regimes. Precipitation albedo has also been revealed to be a crucial parameter when predicting the effective mean temperature, especially for low-to-medium path attenuation. Saturation effects of the effective mean temperature for high rain rate and path attenuation also have been discussed.

Scaling properties, with respect to frequency and angle, also have been taken into consideration and quantified in the microwave and millimeter-wave range. Average frequency dependence of the effective mean temperature may be considerable below K-band, whereas the angle scaling is almost negligible for frequency above K-band and intense rainfall. Statistical prediction methodologies have been developed, exploiting the multiple regression analysis and using slant-path attenuation, columnar liquid water content, and rainfall rate as predictors. The choice of these predictors is due to the fact that rain-gauge and path-attenuation experimental data sets at various frequency bands and for many geographical areas are widely available to the radio-propagation community. On the other hand, the use of numerical outputs of forecast meteorological models, containing columnar liquid water as a common diagnostic variable, is becoming more and more helpful within link-budget design procedures. Polynomial regressive models have been carefully compared and selected and the estimation error has been evaluated, providing regression coefficients for various frequency bands.

Experimental link data have been used to test the proposed physically oriented prediction methodology by resorting to measurements of the ITALSAT satellite ground-station at Pomezia. Combined data from the ITALSAT three-beacon receiver and from a three-channel ground-based microwave radiometer have been investigated. Results have been shown in terms of radiometer antenna noise temperature estimation by using beacon slant-path attenuations as predicting variables. The appreciably good accuracy of the estimates for two rainfall case studies has confirmed the potential of the proposed physically oriented prediction technique.

The parameterized relations, proposed in this paper, may support a more accurate evaluation of a link budget at Ka-band and above. The sky-noise temperature within C/N and gain-to-temperature ratio can be interestingly expressed in terms of other more familiar variables such as attenuation and rain rate. The angle and frequency scaling may allow the extrapolation of results to various link configurations. Future work should be devoted to a systematic validation of the proposed SNEM-based prediction method, using larger measurements data sets for various climates. To this aim, colocated data from a beacon receiver and a microwave radiometer would represent the most

appealing configuration as multifrequency microwave radiometers can provide an independent accurate measurement of the antenna noise temperature, even though usually at a frequency different from beacon receivers. Short-term and long-term statistics of sky-noise temperature at millimeter-wave frequencies, due to clouds and rainfall, could also represent a valuable further scope of this work. Other prediction techniques could be also taken into consideration in order to enhance the overall accuracy of the physically oriented estimation methodology.

ACKNOWLEDGMENT

Data from the ITALSAT station were kindly provided by Dr. A. Martellucci (now at ESA-ESTEC, NL) and Dr. E. Fionda and F. Consalvi of Fondazione Ugo Bordoni, Rome, Italy.

REFERENCES

[1] L. J. Ippolito, "Radio propagation for communications," *Proc. IEEE*, vol. 69, pp. 697–727, Jun. 1981.

[2] D. V. Rogers, L. J. Ippolito, Jr., and F. Davarian, "System requirements for Ka-band propagation effects on earth-satellite links," *Proc. IEEE*, vol. 85, pp. 810–821, 1997.

[3] S. M. R. Jones and P. A. Watson, "Attenuation and countermeasures in millimeter-wave point-to-multipoint networks," *Radio Sci.*, vol. 28, pp. 1057–1069, 1993.

[4] P. A. Watson and Y. F. Hu, "Prediction of attenuation on satellite-earth links for systems operating with low fade margins," *Proc. Inst. Elect. Eng. Microw. Antennas Propag.*, vol. 141, pp. 467–472, 1994.

[5] A. Dissanyake, J. Allnut, and F. Haidara, "A prediction model that combines rain attenuation and other propagation impairments along Earth-satellite paths," *IEEE Trans. Antennas Propag.*, vol. 45, pp. 1546–1558, 1997.

[6] R. K. Crane, "Prediction of attenuation by rain," *IEEE Trans. Commun.*, vol. 28, pp. 1717–1733, 1980.

[7] E. E. Altshuler and R. A. Marr, "Cloud attenuation at millimeter wavelengths," *IEEE Trans. Antennas Propag.*, vol. 37, pp. 1473–1479, 1991.

[8] F. S. Marzano and C. Riva, "Cloud-induced effects on long-term amplitude scintillation along millimeter-wave slant paths," *IEEE Trans. Antennas Propag.*, vol. 51, pp. 880–887, 2003.

[9] M. Filip and E. Vilar, "Adaptive modulation as a fade countermeasure: An Olympus experiment," *Int. J. Sat. Commun.*, vol. 8, pp. 31–41, 1990.

[10] F. S. Marzano, J. Turk, P. Ciotti, S. Di Michele, and N. Pierdicca, "Potential of combined spaceborne microwave and infrared radiometry for near real-time rainfall attenuation monitoring along earth-satellite links," *Int. J. Satell. Commun.*, vol. 19, no. 4, pp. 385–412, 2001.

[11] M. S. Alouini, S. A. Borgsmiller, and P. G. Steffes, "Channel characterization and modeling for Ka-band very small aperture terminals," *Proc. IEEE*, vol. 85, no. 6, pp. 981–997, 1997.

[12] B. R. Arbesser-Rastburg and A. Paraboni, "European research on Ka-band slant path propagation," *Proc. IEEE*, vol. 85, pp. 843–852, 1997.

[13] A. Ishimaru and R. L. -T. Cheung, "Multiple-scattering effect on radiometric determination of rain attenuation at millimeter-wavelengths," *Radio Sci.*, vol. 15, pp. 507–516, 1980.

[14] S. Senin, C. Catalan, and E. Vilar, "Influence of sky noise temperature and propagation phase noise on VSAT design at millimeter-wave frequencies," in *Proc. 3rd Ka Band Utilization Conf.*, Sorrento, Italy, 1997, pp. 401–406.

[15] F. S. Marzano, C. Di Ciero, P. Ciotti, and E. Fionda, "Characterization of ground-based antenna noise temperature due to precipitating clouds from Ku to W band," in *Proc. CLIMPARA-2001, Budapest (H)*, May 2001, pp. 28–30.

[16] International Telecommunication Union—Radiopropagation (ITU-R), Radio noise Geneva, Switzerland, ITU-R Rec., 2001, pp. 372–377.

[17] R. K. Crane, X. Wang, D. B. Westenhaver, and W. J. Vogel, "ACTS propagation experiment: Experiment design, calibration, and data preparation and archival," *Proc. IEEE*, vol. 85, pp. 863–878, 1997.

[18] R. Polonio and C. Riva, "ITALSAT propagation experiment at 18.7, 39.6, and 49.5 GHz at Spino d'Adda: Three years of CPA statistics," *IEEE Trans. Antennas Propag.*, vol. 46, pp. 631–635, 1998.

[19] G. Brussaard and P. A. Watson, *Atmospheric Modelling and Millimetre Wave Propagation*. London, U.K.: Chapman & Hall, 1995.

[20] F. S. Marzano, E. Fionda, and P. Ciotti, "Simulation of radiometric and attenuation measurements along earth-satellite links in the 10- to 50-GHz band through horizontally-finite convective raincells," *Radio Sci.*, vol. 34, pp. 841–858, 1999.

[21] F. S. Marzano and L. Roberti, "Numerical investigation of intense rainfall effects on coherent and incoherent slant-path propagation at K band and above," *IEEE Trans. Antennas Propag.*, vol. 41, no. 5, pp. 965–977, 2003.

[22] F. S. Marzano, "Modeling antenna noise temperature due to rain clouds at microwave and millimeter-wave frequencies," *IEEE Trans. Antennas Propag.*, vol. 54, pp. 1305–1317, 2006.

[23] M. Barkat, *Signal Detection and Estimation*. Norwood, MA: Artech House, 1991.

[24] L. J. Crone, L. M. McMillin, and D. S. Crosby, "Constrained regression in satellite meteorology," *J. Appl. Meteor.*, vol. 35, pp. 2023–2039, 1996.

[25] A. Aresu, E. Damosso, A. Martellucci, L. Ordano, and A. Paraboni, "Depolarization of electromagnetic waves due to rain and ice: Theory and experimental results," *Alta Frequenza*, vol. 6, pp. 70–75, 1994.

Frank S. Marzano (S'89–M'99–SM'03) received the laurea degree *(cum laude)* in electrical engineering and the Ph.D. degree (1993) in applied electromagnetics from the University of Rome La Sapienza, Italy, in 1988 and 1993, respectively.

In 1993, he collaborated with the Institute of Atmospheric Physics, CNR, Rome. From 1994 to 1996, he was with the Italian Space Agency, Rome, as a Postdoctorate Researcher. After being a Lecturer at the University of Perugia, Italy, in 1997 he joined the Department of Electrical Engineering and cofounded the Center of Excellence CETEMPS, University of L'Aquila, Italy, coordinating the Satellite and Radar Remote Sensing Laboratory. In 2005, he joined the Department of Electronic Engineering, University of Rome La Sapienza, where he presently teaches courses on antennas, propagation, and remote sensing. He has published more than 65 papers in international refereed journals and more than 120 extended abstracts in conference proceedings. His current research concerns passive and active remote sensing of the atmosphere from ground-based, airborne, and spaceborne platforms, with a particular focus on precipitation using microwave and infrared data, development of inversion methods, radiative transfer modeling of scattering media, and radar meteorology issues. He is also involved in radiopropagation topics in relation to incoherent wave modeling, scintillation prediction, and rain fading analysis along satellite microwave links. Since 2001, he has been the Italian National Delegate for the European COST actions n.720 on atmospheric profiling by ground-based remote sensing and n.280 on satellite fade mitigation techniques.

Dr. Marzano is a member of the Italian Society of Electromagnetics (SIEM). He received the Young Scientist Award from the XXIV General Assembly of the International Union of Radio Science in 1993. In 1998, he received the Alan Berman Publication Award from the Naval Research Laboratory, Washington, DC. Since January 2004, he has been an Associate Editor of IEEE GEOSCIENCE REMOTE SENSING LETTERS. In 2004 and 2006, he was Co-Guest Editor of special issues on MicroRad for IEEE TRANSACTIONS ON GEOSCIENCE AND REMOTE SENSING.